Pergamon

Acta mater. 49 (2001) 2761–2772

Acta MATERIALIA

www.elsevier.com/locate/actamat

ON AN ELASTICALLY INDUCED SPLITTING INSTABILITY

P. H. LEO[1]†, J. S. LOWENGRUB[2, 3] and Q. NIE[4]

[1]Department of Aerospace Engineering and Mechanics, University of Minnesota, Minneapolis, MN 55455 USA, [2]School of Mathematics, University of Minnesota, Minneapolis, MN 55455, USA, [3]Department of Mathematics, University of North Carolina, Chapel Hill, NC 27599 USA and [4]Department of Mathematics, University of California at Irvine, Irvine, CA 92697 USA

(Received 28 December 2000; received in revised form 10 April 2001; accepted 10 April 2001)

Abstract—We show that a morphological instability driven by deviatoric applied stresses can generate elastically induced particle splitting during diffusional phase transformations. The splitting instability occurs when the elastic fields are above some critical value. For subcritical elastic fields, one observes a small perturbation of the particle shape consistent with splitting, but this perturbation is stabilized by surface tension. Both the onset of the splitting instability and the nonlinear evolution of the particle towards splitting depend on the precise form of the applied stress, the elastic constants of the precipitate and matrix, and the initial shape of the precipitate. We also investigate whether non-dilatational misfit strains can generate splitting instabilities in the absence of an applied stress. © *2001 Acta Materialia Inc. Published by Elsevier Science Ltd. All rights reserved.*

Keywords: Theory & modeling; Phase transformations; Stress

1. INTRODUCTION

In this paper, we consider the elastically induced splitting of precipitates that arise during phase transformations in the solid state. It is well known that elastic stresses that arise during solid state phase transformations in some alloys can lead to microstructural features such as precipitate alignment (rafting), cuboidal precipitate shapes and particle splitting. There has been a wealth of experimental work on nickel-based model superalloys documenting how the mismatch strain between the precipitate and surrounding matrix phase changes the characteristics of the microstructure [1–6]. At the same time, theoretical work and numerical simulations have revealed how physical features such as elastic anisotropy, inhomogeneous elastic constants, ordering and lattice constant mismatch affect both the kinetics of microstructure formation and the equilibrium microstructure; see for example [7–20] for a small sampling of the literature.

One of the primary reasons for considering the role of elasticity in microstructure formation is that it offers the possibility of using elastic stresses to design desirable microstructures. In this context, one of the possibilities that is often cited is that of inverse coarsening. In inverse coarsening, the elastic fields would promote the growth of a small precipitate at the expense of a larger neighbor——exactly opposite to surface energy driven coarsening. In principle, then, elasticity could favor an array of equally sized precipitates, which would lead to improved mechanical properties of the alloy.

The observed elastic effect that is perhaps most closely linked to inverse coarsening is particle splitting. Particle splitting is a process in which one cuboidal particle splits into several particles, usually two (a doublet) or eight (an octet). Such splitting has been observed experimentally [3, 21, 4, 6] and has been theoretically identified as an elastically driven process [22, 11, 13].

While splitting may be an important factor for inverse coarsening, the precise experimental and theoretical conditions under which it occurs are not completely clear. The mechanism of the splitting is similarly unclear. Some experimental pictures suggest that splitting occurs via a morphological instability in which the sides of a cuboidal precipitate become increasingly concave until splitting occurs, see e.g. [6]. Other pictures suggest a hollowing at the center of the particle, see e.g. [22]. There have also been many theoretical simulations of splitting using diffuse interface techniques that suggest that the instability occurs by the “hollowing” mechanism, see e.g. [19,

† To whom all correspondence should be addressed. Fax: +1-612-626-1558

E-mail address: phleo@aem.umn.edu (P. H. Leo)

PII: S1359-6454(01)00179-3

23, 13]. Recently, Lee, using a discrete atom method, has observed splitting by an instability mechanism [24–26].

A common observation of Lee's work and the diffuse interface calculations of Li and Chen [13] is that applied fields may contribute to the instability. Here, we follow that trail and show that splitting can occur via an elastically induced morphological instability driven by an applied stress. More precisely, we find that applied stress can generate a splitting instability, if it has some deviatoric component. The splitting instability also requires that the ratio of the elastic energy to surface energy be above some critical level. Details of the instability, such as the direction of splitting, depend on the applied field, the misfit strain, and the elastic constants of the two phases.

In Section 2, we present the coupled diffusion/elasticity system used to calculate the microstructural evolution. We also give a brief summary of the numerical methods used to solve the problem, based on previous work [9, 10]. In Section 3 we present numerical results that show the splitting instability for different applied stresses and elastic constants. In Section 4 we discuss the results, and consider whether similar splitting instabilities can be generated by misfit strain alone.

2. FORMULATION

2.1. Governing equations

Consider a system consisting of an isolated precipitate surrounded by a matrix. Both phases are binary mixtures. We denote by c the normalized composition of the mixture in the matrix. The analogous composition in the precipitate is denoted by c^P and is assumed to be constant. (A full set of dimensionless variables is given in Appendix A) The entire system occupies the two dimensional plane R^2 with the precipitate occupying the finite area Ω^P. The precipitate-matrix interface is denoted Γ.

The precipitates evolve by diffusion of solute through the matrix phase, with elastic interactions occurring through the diffusion fields. Diffusion in the matrix is assumed to be quasi-static, so

$$\Delta c = 0 \text{ in } \Omega^M. \tag{1}$$

The boundary condition for the matrix composition at the precipitate-matrix interface is the generalized Gibbs-Thomson condition [27, 9, 28], which in normalized form can be written as

$$c = \kappa + ZG^{el} \text{ on } \Gamma. \tag{2}$$

where κ is the mean curvature of the interface, and G^{el} is an elastic energy density defined by equation (14) below. Also,

$$Z = \frac{C_{66}^M(\varepsilon_{22}^T)^2 R}{\gamma} \tag{3}$$

characterizes the relative contribution of the elastic and surface energies, with C_{66}^M an elastic modulus of the matrix in Voight notation, ε_{22}^T the 22 component of the misfit strain†, R a characteristic length scale and γ the surface energy. Note that with this choice for Z, stresses are normalized by the quantity $C_{66}^M\varepsilon_{22}^T$ (see Appendix A).

We take the system to be closed with respect to mass flux:

$$\lim_{R_\infty \to \infty} \frac{1}{2\pi} \int_{\Gamma_\infty} \nabla c \cdot \mathbf{n}\, ds = 0 \tag{4}$$

where R_∞, is the radius of a circle enclosing the precipitate. The fact that the mass flux into the system vanishes implies that the total area of the precipitate remains fixed. We remark that dendritic instabilities have been observed when there is mass flux into the system [9]. Finally, the normal velocity V of the precipitate-matrix interface is computed through a flux balance at the interface as

$$V = \nabla c \cdot \mathbf{n}|_\Gamma \tag{5}$$

We next discuss the elasticity problem. In order to determine the elastic energy density G^{el} used in equation (2) we must compute the elastic fields on the interface Γ. We make the following assumptions in order to calculate the elastic fields: (1) both the precipitate and matrix phases are linear elastic with orthotropic symmetry; (2) elastic fields arise because of misfit strains between the precipitate and matrix phases as well as far-field applied stresses; (3) the precipitate-matrix interfaces are coherent, so both displacement and traction are continuous across interfaces; and (4) elastic equilibrium (with zero body force) applies at every stage in the evolution of the precipitates. Then, the governing equations can be written (using indicial notation with summation convention),

$$\sigma_{ij,j}^\chi = 0 \text{ in } \Omega^{\chi = M,P} \ (i,j = 1,2) \tag{6}$$

$$u_i^P = u_i^M \text{ on } \Gamma \ (i,j = 1,2) \tag{7}$$

$$t_i^P = \sigma_{ij}^P n_j = \sigma_{ij}^M n_j = t_i^M \text{ on } \Gamma \ (i,j = 1,2) \tag{8}$$

with far-field condition

† Any non-zero component may be used for the scaling.

$$\lim_{r\to\infty}\sigma_{ij}^{M} = \sigma_{ij}^{O} \tag{9}$$

where σ_{ij}^{O} is the applied far-field stress. The displacement is required to be finite throughout the system. The constitutive relations between the stress σ and the strain ε are given by

$$\sigma_{ij}^{P} = C_{ijkl}^{P}(\varepsilon_{kl}^{P} - \varepsilon_{kl}^{T}) \tag{10}$$

in the precipitate, where ε_{ij}^{T} denotes the misfit strain, and

$$\sigma_{ij}^{M} = C_{ijkl}^{M}\varepsilon_{kl}^{M} \tag{11}$$

in the matrix. In equation (10) and equation (11), the strain components ε_{ij} are computed from the displacement components u_i by

$$\varepsilon_{ij} = \frac{1}{2}(u_{i,j} + u_{j,i}) \tag{12}$$

in both the matrix and precipitate. Also, C^P and C^M denote the stiffness tensors of the precipitate and matrix phases respectively, which in Voight notation have the form

$$C = \begin{pmatrix} C_{11} & C_{12} & 0 \\ C_{12} & C_{22} & 0 \\ 0 & 0 & C_{66} \end{pmatrix} \tag{13}$$

for the two-dimensional case with orthotropic symmetry considered here. We remark that if a phase has cubic symmetry, then $C_{11} = C_{22}$.

Finally, once the elasticity problem is solved, G^{el} is computed as

$$G^{el} = \frac{1}{2}\sigma_{ij}^{P}(\varepsilon_{ij}^{P} - \varepsilon_{ij}^{T}) - \frac{1}{2}\sigma_{ij}^{M}\varepsilon_{ij}^{M} + \sigma_{ij}^{M}(\varepsilon_{ij}^{M} - \varepsilon_{ij}^{P}) \text{ on } \Gamma \tag{14}$$

2.2. Boundary integral formulation and numerics

Both the diffusion and elasticity problems are reformulated as boundary integral equations and solved numerically. Complete details are given in [9, 29]; here we give only the key ideas.

The reformulation of the elasticity problem through boundary integrals is based on the fundamental solution to orthotropic elasticity in two-dimensions given by Green [30], see also Rizzo and Shippy [31] and Schmidt and Gross [32, 16, 33]. We note that using this fundamental solution requires that $2C_{66}/(\sqrt{C_{11}C_{22}} - C_{12}) \leq 1$. For cubic systems, this combination of elastic constants reduces to the anisotropy ratio $A = 2C_{66}/(C_{11} - C_{12})$ and so the restriction is $A \leq 1$. However, by rotating the cubic coordinate system by $\pm\pi/4$, one maps $A \to 1/A$ while preserving the cubic structure of the stiffness and compliance tensors. Thus the restriction on elastic constants for the two-phase problem with cubic anisotropy becomes that both phases must have either $A > 1$ or $A < 1$. It is important to note that this mapping does not work for general orthotropic systems, as rotations create non-orthotropic structure in the stiffness and compliance tensors.

Given the fundamental solution for orthotropic elasticity, the formulation of the boundary integral equation for the two-phase problem proceeds as in the isotropic case discussed in [9]. One uses the fundamental solution to write the displacement u_j at a point $\boldsymbol{x}(s)$ on Γ in terms of a principal value integral involving the fundamental solution as well as the displacements and tractions at all point $\boldsymbol{x}'(s)$ on Γ. This is done from both sides of the interface——on the precipitate side the misfit strain enters through equation (10), while on the matrix side the far-field strain enters from equation (9). Continuity of displacement and traction on the interface couples the two boundary integrals, leading to a set of boundary integral equations that can be solved for the displacements and tractions on the interface. The displacements and tractions on the interface can then be used together with the fundamental solution to find the elastic fields everywhere in the system; however we only need these fields on the interface to compute G^{el}.

Once G^{el} is determined, the diffusion problem is completely specified. This problem is also solved in terms of boundary integrals. Following [34, 29], one introduces a dipole density on Γ as well as p (for p precipitates) source terms to account for far-field flux. This formulation automatically solves Laplace's equation. Matching the boundary condition (2) and far-field flux condition (4) leads immediately to a set of boundary integrals that can be solved for the dipole density and source strengths and hence the full composition field. Finally, the normal velocity can be computed by using the Dirichlet-Neumann map, see [9, 29].

The integral equations for both elasticity and diffusion are solved by using the collocation method together with the iterative solver *GMRES* [35]. The matrix system for the elasticity is preconditioned following [9], and the system for the diffusion problem is preconditioned using the method of Greenbaum *et al.* [29]. The integrals are calculated by alternating point quadratures [36]. Any derivatives or anti-derivatives are obtained using the FFT. Finally, following [9, 37], a 25th order Fourier filter is employed to reduce aliasing errors.

To evolve the precipitate-matrix interface Γ, we use a formulation based on the tangent angle θ (measured counterclockwise from the horizontal) and the area A of a precipitate [9, 37]. An artificial tangential velocity T is used so that computational points on the interface are equally spaced in arclength at all times. The resulting equations for the motion of the interface are numerically stiff because of the surface energy; however, an advantage of using the scaled arclength formulation is that it is straightforward to develop non-stiff time integration schemes. Here, for example, we use an integrating factor approach developed by [37, 9] to remove the stiffness, and solve the resulting equations using an explicit time integration scheme.

To summarize, implementation of the code requires that at each time step, we (1) solve the integral equations for elasticity to obtain G^{el} on Γ; (2) solve the integral equations for diffusion to find the composition and its normal derivative on Γ; (3) calculate the normal velocity of Γ; and (4) update Γ. Each step (1)-(3) has computational cost $O(M^2)$ for M grid points on Γ, while step (4) is $O(M)$. The elastic solver is particularly costly as there are $4M$ unknowns associated with elasticity (two displacement components and two traction components). Hence steps (1)-(3) are implemented in parallel while step (4) is implemented sequentially. The computations were run using a SGI Origin-2000, and a typical computation showing a splitting instability takes between 4 and 8 hours using 2048 grid points and 4 processors. In general, we were able to resolve shapes using 1024 or 2048 grid points on an interface, though more points are used when shapes exhibit high curvatures.

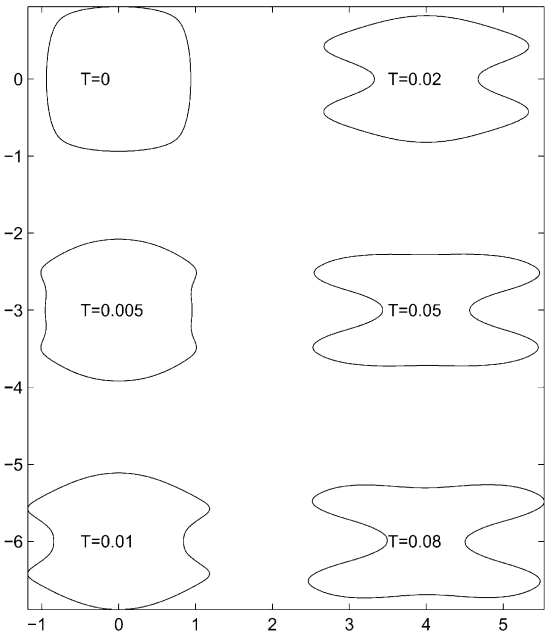

Fig. 1. The evolution of a Ni_3Ga precipitate under an applied shear stress $\sigma^0_{11} = 1$, $\sigma^0_{22} = -1$ and $\sigma^0_{12} = 0$. The misfit is dilatational ε^T=1, Z=5 and the initial shape is the equilibrium shape for a Ni_3Ga with dilatational misfit only.

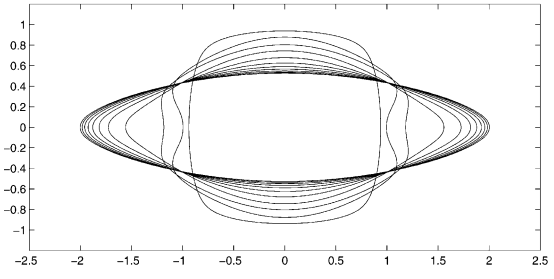

Fig. 2. The evolution of a Ni_3Ga precipitate under an applied shear stress $\sigma^0_{12} = 1$, $\sigma^0_{22} = -1$ and $\sigma^0_{12} = 0$. The misfit is dilatational, ε^T=1, Z=3 and the initial shape is the equilibrium shape for a Ni_3Ga with dilatational misfit only.

3. RESULTS

We have found that non-dilatational applied stresses can generate a morphological instability that will eventually cause particle splitting. We have also seen a similar tendency towards splitting, generated by a non-dilatational misfit strain; however we have been unable to follow this instability far enough to assert that the particle will indeed split. In the following we begin by considering non-dilatational applied stresses, and we then look at non-dilatational misfit strains.

3.1. Applied stresses

3.1.1. Elastically soft particles. Figures 1 and 2 show the evolution of a particle with elastic constants appropriate to Ni_3Ga embedded in a matrix with the elastic constants of Ni (see Table 1). Note that the elastic constants of Ni_3Ga are smaller than those of Ni; in this case the precipitate is referred to as elastically soft. The misfit strain is dilatational, $\varepsilon^T_{ij} = \delta_{ij}$, and the applied field is a shear with $\sigma^0_{11} = 1$, $\sigma^0_{22} = -1$, and $\sigma^0_{12} = 0$. In Fig. 1, $Z = 5$, while in Fig. 2, $Z = 3$.

In both figures, the particle evolves from an initial shape that corresponds to the equilibrium shape of a Ni_3Ga particle in the absence of applied stress. This shape was found by evolving from a circle until the composition on the interface is uniform (we note that there is another, less symmetric, equilibrium shape for this value of Z [10, 16]). When the far-field stress is applied, one observes an initial instability in the form of a concave region forming from the left and right surfaces of the particle. When $Z = 5$, Fig. 1, this initial instability grows in such a way that it splits the particle into two horizontal plates stacked on top of each other. (Because our numerical method tracks mathematically sharp interfaces, we cannot follow the actual separation of the particles; however this separation can be tracked using diffuse interface methods [28, 15].) On the other hand, when $Z = 3$, Fig. 2, the initial instability is stabilized by the (relatively) higher value of the surface energy. This shows that the instability is in fact driven by elasticity. For the

Table 1. Normalized elastic constants used in the simulations

	C_{11}	C_{12}	C_{22}	C_{66}
Nickel	2.03	1.21	2.03	1.0
Ni_3Al	1.83	1.21	1.83	1.02
Ni_3Ga	1.54	0.996	1.54	0.87
Ni_3Si	3.04	1.62	3.04	1.35

$Z = 3$ case the precipitate evolves towards its equilibrium (plate-like) shape.

One can also track the instability by looking at the evolution of the elastic energy ZG^{el} and the curvature κ associated with the precipitate-matrix interface. These quantities are shown in Fig. 3 for the two simulations above. The abscissa in these plots is the scaled arclength parameter α along the interface, where $\alpha = 0$ is on a line 45° from the horizontal and α increases counterclockwise. The curves at time $t = 0$ are computed just after the applied stress is applied, and so $\kappa + ZG^{el}$ is far from uniform. The only difference in the two cases at $t = 0$ is the magnitude of ZG^{el}. As time progresses, one observes that G^{el} and κ roughly mirror each other, as the particle evolves towards equilibrium. When $Z = 5$, G^{el} forms two sharp upward spikes that are countered by downward spikes in κ. These correspond to the pinching instability (concavity) on the left and right sides of the particle. There is a similar structure to G^{el} and κ

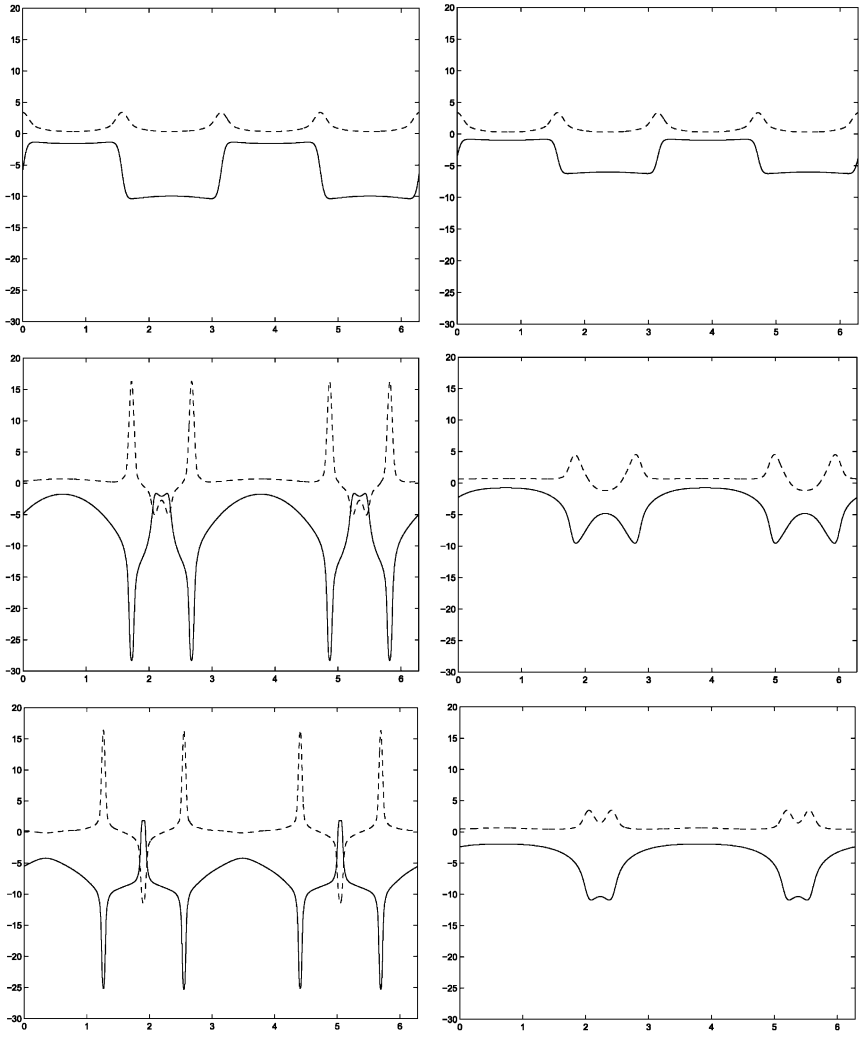

Fig. 3. The curvature κ (dashed) and elastic energy $Z{\cdot}G^{el}$ (solid) on the interface plotted versus scaled arclength along the interface. The particle has Ni_3Ga elastic constants, applied field $\sigma^0_{11} = 1$, $\sigma^0_{12} = 0$, $\sigma^0_{22} = -1$ and dilatational misfit ε^T=1. The plots in the left column are for Z=5 (splitting) while the plots in the right column are for Z=3 (no splitting). The scaled arclength parameter is zero on a line 45° from the horizontal and increases counterclockwise.

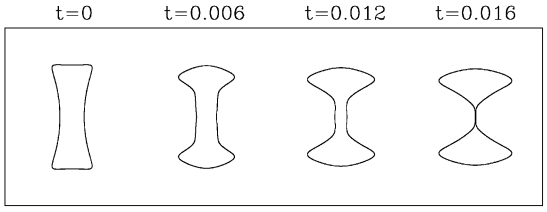

Fig. 4. The evolution of a Ni_3Ga precipitate under an applied shear stress $\sigma^0_{11} = 1$, $\sigma^0_{22} = -1$ and $\sigma^0_{12} = 0$. The misfit is dilatational, ε^T=1, Z=3 and the initial shape is a dog-bone.

when $Z = 3$, however the spikes are much less strong, and so there are only small regions of concavity at $t = 0.02$, and none at $t = 0.05$.

We have observed that the direction of the instability corresponds to whether the equilibrium shape for a given applied stress, misfit and precipitate and matrix elastic constants, is a plate oriented horizontally (as in Fig. 1) or vertically. It is convenient to study the splitting instability by using this observation to choose an initial shape that favors the instability; hence we have done extensive simulations with a "dog-bone" initial shape. This shape can be used to enhance the splitting by orienting the long axis of the dog-bone perpendicular to the direction of splitting; equivalently, perpendicular to the long axis of the equilibrium shape. Conversely, the dog-bone shape will prevent splitting if it is oriented along the long axis of the equilibrium shape.

Figure 4 shows a vertical dog-bone initial shape chosen to enhance the splitting process of soft Ni_3Ga precipitates. The applied stress is the same as in Figs. 1 and 2, namely, $\sigma^0_{11} = 1$, $\sigma_{22} = -1$ and $\sigma^0_{12} = 0$. As expected, for $Z = 5$ the instability proceeds rapidly as the particle forms a thin vertical neck between two horizontal plate-shaped particles. By plotting the neck distance of the precipitate as a function of time (Fig. 5), we find that in the final stages of pinching the neck distance decreases roughly linearly in time. In contrast to the situation in Fig. 2, where an initially circular shape is stable when $Z = 3$, the dog-bone initial shape is unstable and will split when $Z = 3$. However, when Z is reduced to 1, the dog-bone evolves towards a single horizontally oriented plate, as in Fig. 2.

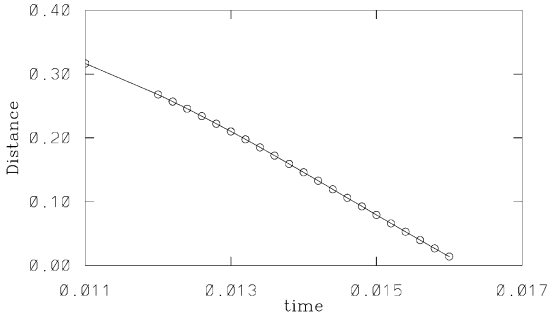

Fig. 5. The neck width as a function of time for the Ni_3Ga precipitate shown in Fig. 4.

For a given initial shape, the onset of the instability depends on the magnitude of both the misfit (through the parameter Z) and the applied stress. We have repeated the calculation shown in Fig. 4 with different values of Z and applied shear in order to determine the critical values associated with the splitting instability. For example, when $Z = 5$, splitting occurs when $\sigma^0_{11} = -\sigma^0_{22}$ falls between 0.45 and 0.475. As Z increases, the critical applied shear falls in the ranges 0.275-0.3 for $Z = 10$, 0.225-0.25 for $Z = 20$ and 0.175-0.2 for $Z = 25$. Conversely, one could fix the applied shear $\sigma^0_{11} = -\sigma^0_{22} = 1$ and determine the value of Z required to generate splitting. It is interesting to note that for the applied shear case, the combination $\sqrt{Z}\sigma^0$, which scales the interaction energy between the misfit and applied field, is roughly constant (near unity) for all the critical points we have identified.

The form of the applied stress will also affect the onset and evolution of a splitting instability. An immediate observation is that changing the sign of either the applied stress or misfit strain changes the direction of the splitting. For example, if the sign of either the applied stress or misfit strain used in Fig. 1 is changed, then one finds that the particles split into vertical plates. If one changes the sign of both the applied stress and misfit strain, the figure is unchanged. Similar conclusions may be made for the dog-bone initial shape if the initial shape is rotated appropriately.

It is also interesting to consider different applied stresses, and in particular uniaxial stresses. Figure 6 shows a soft precipitate with Ni_3Ga elastic constants, $Z = 5$, a uniaxial load $\sigma^0_{11} = 1$ and a positive dilatational misfit. As in Fig. 4, the particle develops a splitting instability such that it will eventually form two horizontal plates. The rate of necking under uniaxial loads is roughly five times slower than the shear

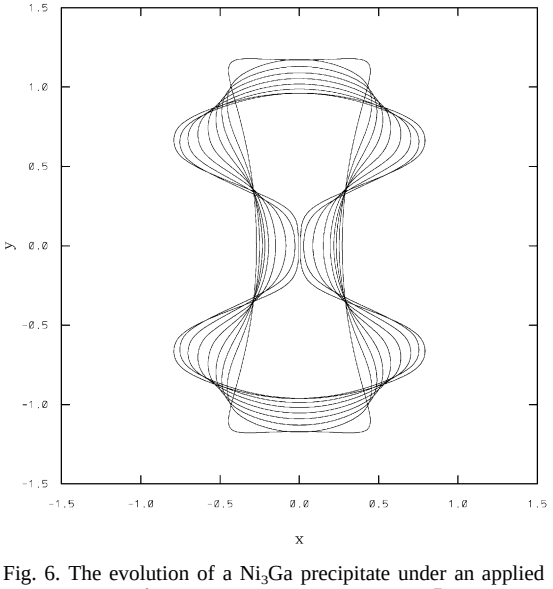

Fig. 6. The evolution of a Ni_3Ga precipitate under an applied uniaxial stress $\sigma^0_{11} = 1$. The misfit is dilatational, ε^T=1, Z=5 and the initial shape is a dog-bone.

load $\sigma^0_{11} = 1$, $\sigma^0_{22} = -1$, $\sigma^0_{12} = 0$ shown in Fig. 4. We note that the dog-bone will also develop a splitting instability under a uniaxial compression in the Z-direction. However, applied stresses $\sigma^0_{11} = -1$ or $\sigma^0_{22} = 1$ will not lead to splitting, as both the applied fields and the initial shape favor a vertically oriented plate.

3.1.2. Elastically hard particles. We next consider the evolution of a particle with elastic constants corresponding to Ni_3Si embedded in a matrix with the elastic constants of Ni. In this case the elastic constants of the particle are larger than those of the matrix (see Table 1); this case is referred to as elastically hard. Figure 7 shows the evolution of a precipitate using the same applied stress and misfit strain as in Fig. 1, i.e., $\varepsilon^T_{ij} = \delta_{ij}$, $\sigma^0_{11} = 1$, $\sigma^0_{22} = -1$ and $\sigma^0_{12} = 0$. In this case, the initial shape is the equilibrium shape of a Ni_3Si particle with a dilatational misfit strain and under no applied stress. As in the soft particle case, after applying the shearing stress, we observe a splitting instability. The instability now emerges from the top and bottom of the particle and so splits the particle into two vertical plates oriented side by side. The fact that this is an elastically induced instability is confirmed by decreasing the parameter Z while keeping the other parameters fixed. Figure 8 shows the particle evolution with $Z = 3$. The initial perturbation is clearly seen, but at some point it stabilizes and the particle grows towards a single vertical plate.

In general the results for hard particles are similar to those for soft particles, except that (all else being equal) an instability will be rotated 90° relative to the soft particle case. There are, however, some clear differences between the instabilities of hard and soft particles. The first is related to the precise shape of the neck region and the rate of necking. Figure 9 shows the evolution of a Ni_3Si particle with a dog-bone initial shape, $Z = 5$, $\sigma^0_{11} = -1$ and $\varepsilon^T_{ij} = \delta_{ij}$. This figure compares to Fig. 6 for a soft particle, with the sign of the applied stress chosen so that splitting occurs horizontally in both cases. The insert in Fig. 9 shows a close-up of the neck region near pinching. Notice that the two sides of the neck form relatively sharp points as they approach each other. In contrast, examination of the neck region in Fig. 6 shows that the neck stays fairly flat as it thins. Figure 10 presents the rate of necking corresponding to Fig. 9. In contrast to the soft particle case, the rate of necking for splitting of hard particles is much faster than linear.

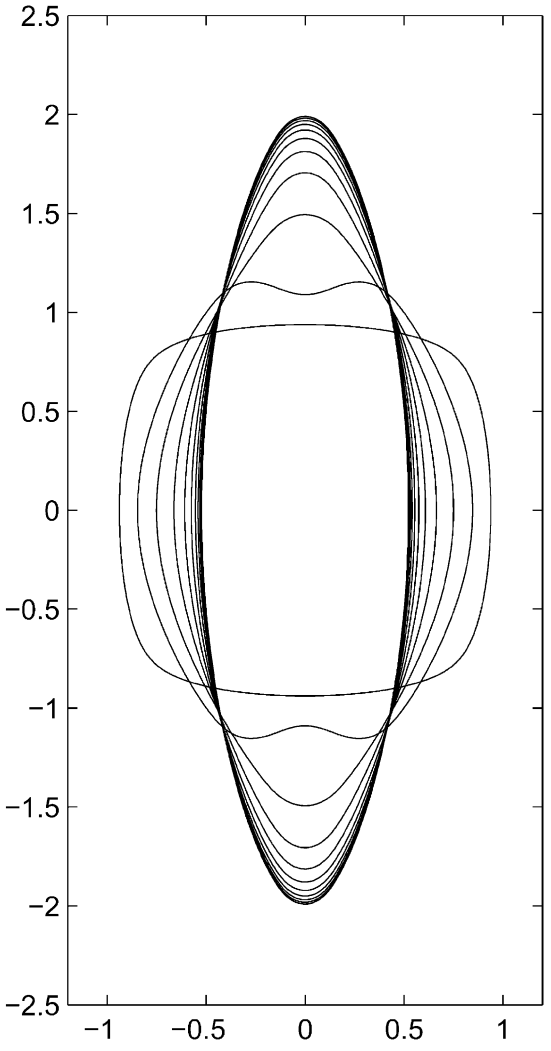

Fig. 8. The evolution of a Ni_3Si precipitate under an applied shear stress $\sigma^0_{11} = 1$, $\sigma^0_{22} = -1$ and $\sigma^0_{12} = 0$. The misfit is dilatational, ε^T=1, Z=3 and the initial shape is the equilibrium shape for a Ni_3Si particle under dilatational misfit only.

These results can be explained by comparing them

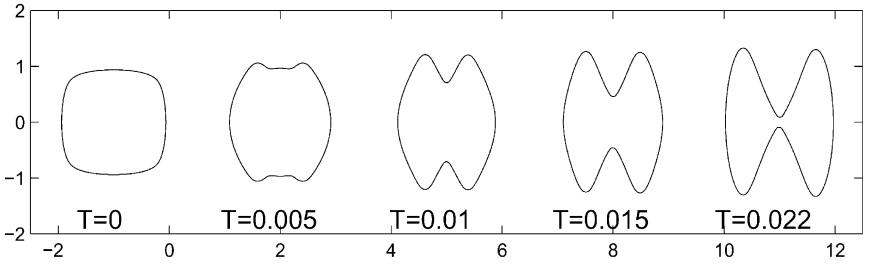

Fig. 7. The evolution of a Ni_3Si precipitate under an applied shear stress $\sigma^0_{11} = 1$, $\sigma^0_{22} = -1$ and $\sigma^0_{12} = 0$. The misfit is dilatational, ε^T=1, Z=5 and the initial shape is the equilibrium shape for a Ni_3Si particle under dilatational misfit only.

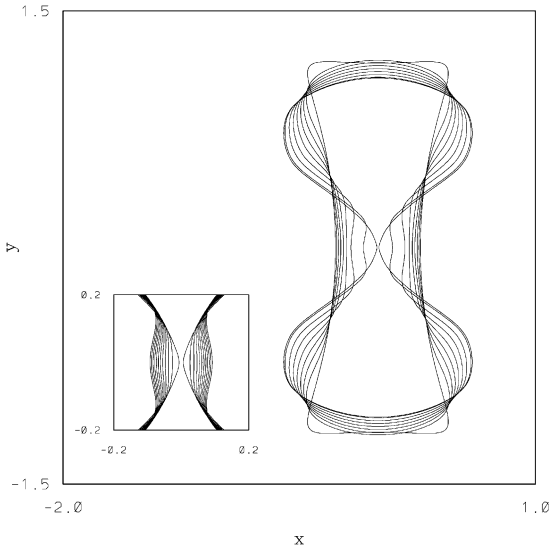

Fig. 9. The evolution of a Ni_3Si precipitate under an applied uniaxial stress $\sigma^0_{11} = -1$. The misfit is dilatational, ε^T=1, Z=5 and the initial shape is a dog-bone. The inset shows a close-up of the neck region.

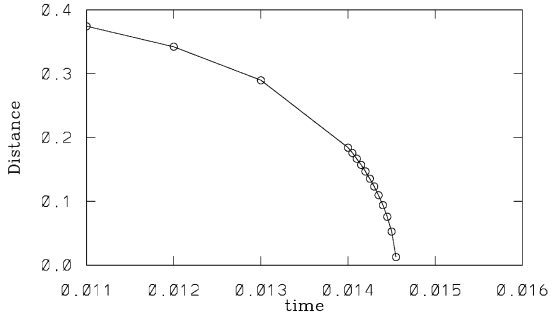

Fig. 10. The neck distance as a function of time for the Ni_3Si precipitate shown in Fig. 9.

to the two particle calculations of Leo *et al.* [10]. Their results show that soft particles have an attractive elastic interaction such that they form points when they are near each other, while hard particles have a repulsive elastic interaction and form flat regions when they are near each other. Hence in the present case, the structure of the neck is determined by whether the matrix material on either side of the neck has attractive interactions (when the matrix is elastically soft) or repulsive interactions (when the matrix is elastically hard). The same considerations explain why pinch-off is faster for hard particles than for soft particles.

Figure 11 shows an interesting higher order instability that only occurs when the particles are hard. The figure shows Ni_3Si dog-bone particles with $Z = 5$ and applied shears $\sigma^0_{11} = -\sigma^0_{22} = -0.7$, $\sigma^0_{11} \equiv \sigma^0_{22} = -0.85$, and $\sigma_{11} = -\sigma_{22} = -1$ ($\sigma^0_{12} = 0$ in all cases). One sees waves form along the sides of the particles prior to splitting, with the number of "waves" increasing from two to four as the magnitude

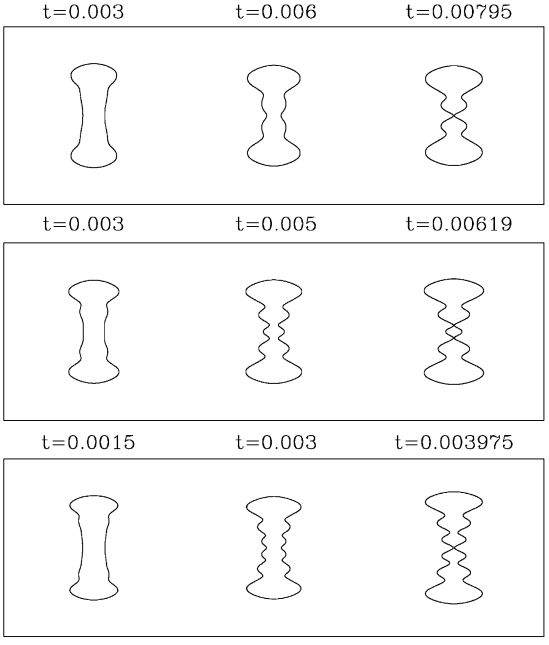

Fig. 11. The evolution of three Ni_3Si precipitates under applied shear stress $\sigma^0_{11} = -\sigma^0_{22} = -\omega$, $\sigma^0_{12} = 0$, with ω=0.7, 0.85 and 1 from top to bottom. In all cases, the misfit is dilatational, ε^T=1, Z=5 and the initial shape is a dog-bone.

of the applied shear increases. Also, it appears that in the intermediate shear case, $\sigma^0_{11} = -\sigma^0_{22} = -0.85$, there are two pinch-off points, suggesting that the particle may split into three.

3.2. Misfit strains

We have also found evidence that a splitting type instability can be generated by non-dilatational misfit strains, though we have been unable to fully track the instability. Figure 12 shows a case of an initially circular particle with tetragonal misfit strains $\varepsilon^T_{11} > \varepsilon^T_{22} = 1$ and $\varepsilon^T_{12} = 0$. The precipitate has the elastic constants of Ni_3Ga and the matrix has the elastic constants of Ni. When $\varepsilon^T_{11} = 1.3$, Fig. 12(a), the particle develops concave regions on its left and right sides. These concave regions rapidly disappear and the particle evolves to an ellipse with long axis in the 1-direction. When ε^T_{11} is increased to 1.5, Fig. 12(b), concave regions form so that the particle assumes a squarish shape, with high curvatures at the corners. Figure 12(c) shows a plot of half the minimum distance between the left and right sides of the particle versus time for both $\varepsilon^T_{11} = 1.3$ and $\varepsilon^T_{11} = 1.5$. The half-length decreases at early times for both values of ε^T_{11}, consistent with the formation of the concave faces. There is a minimum half-length in both cases, suggesting that splitting will not occur when $\varepsilon^T_{11} = 1.5$. However, we are unable to continue the calculation for $\varepsilon^T_{11} = 1.5$ because of difficulty in resolving the shape. While the faster initial decrease of the half-length when $\varepsilon^T_{11} = 1.5$ leaves open the possibility that splitting may occur for larger values of ε^T_{11}, these cases are difficult to resolve.

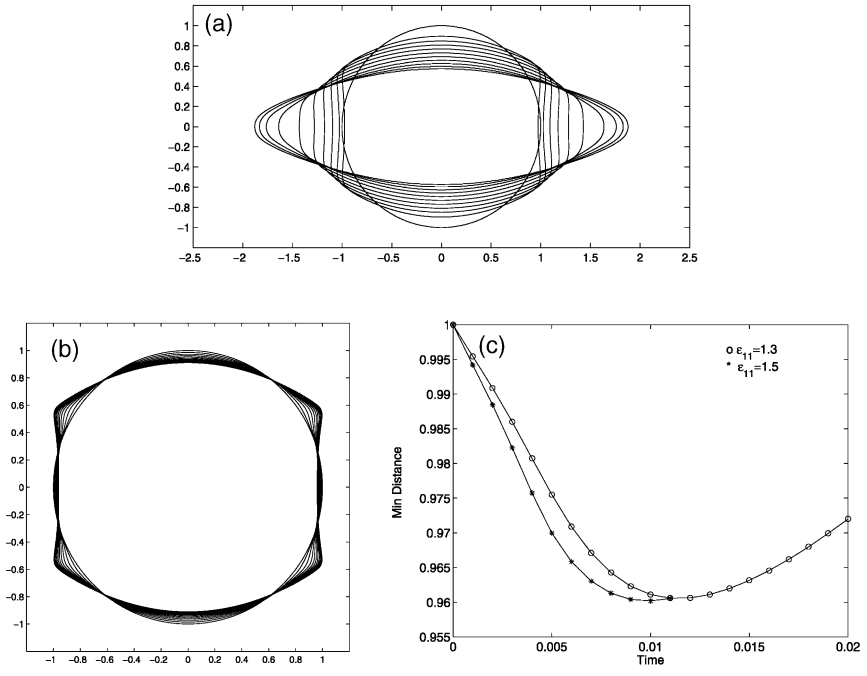

Fig. 12. The evolution of Ni_3Ga precipitates with tetragonal misfit, Z=5 and no applied stress. In (a), $\varepsilon^T_{11} = 1.3$, $\varepsilon^T_{22} = 1$ and $\varepsilon^T_{12} = 0$, while in (b), $\varepsilon^T_{11} = 1.5$, $\varepsilon^T_{22} = 1$ and $\varepsilon^T_{12} = 0$. (c) shows the minimum half length between the left and right sides of the particle corresponding to the shape evolution shown in (a) and (b).

In the absence of applied stress, changing the elastic constants of the particle to those of Ni_3Si has almost no impact on the evolution of the particle. In particular, the evolution of a initially circular Ni_3Si particle with tetragonal misfit $\varepsilon^T_{11} = 1.3$, $\varepsilon^T_{22} = 1$, $\varepsilon^T_{12} = 0$ shows behavior similar to that shown in Fig. 12(a); the particle evolves towards an ellipse with long axis in the 1-direction. This is in contrast to the applied stress case, where the elliptical equilibrium shapes for Ni_3Ga and Ni_3Si particles under the same applied stress (and in the absence of splitting) had different directions of their long axes, see for example Fig. 2 and Fig. 8. Increasing the tetragonality above some critical level again leads to a squarish shape that may be associated with splitting.

We next consider combining non-dilatational applied stress and misfit strains. Figure 13(a) shows a Ni_3Ga particle with misfit $\varepsilon^T_{11} = 1.3$, $\varepsilon^T_{22} = 1$, $\varepsilon^T_{12} = 0$, $Z = 5$ and shear applied stress $\sigma^0_{11} = 1$, $\sigma^0_{22} = -1$, $\sigma^0_{12} = 0$. The initial shape is a circle. We note that the applied stress alone is enough to generate a splitting instability similar to that seen in Fig. 1. With both the misfit strain and applied stress, the particle does not split, but rather evolves toward a diamond-shape, with long axis in the 1-direction. At early times, a sharp nose associated with two kinks appears on the left and right sides of the particle. Facetting proceeds as the kinks move towards the top and bottom of the particle. The remaining facets have normals at roughly $\pm 60°$ and $\pm 120°$ from the horizontal. Figure 13(b) shows a Ni_3Ga particle with misfit $\varepsilon^T_{11} = 1.3$, $\varepsilon^T_{22} = 1$, $\varepsilon^T_{12} = 0$, $Z = 5$ and applied shear stress $\sigma^0_{11} = -1$, $\sigma^0_{22} = 1$, $\sigma^0_{12} = 0$. In this case the applied stress alone leads to splitting with two particles oriented vertically (i.e., a 90° rotation from Fig. 1). When tetragonal misfit strain is introduced, we find that the particle evolves towards a rectangular shape with long axis oriented vertically. The facets have normals in the ±1-directions, while the top and bottom faces have regions of negative curvature.

4. DISCUSSION

We have shown that particle splitting can occur by a morphological instability in the presence of deviatoric applied stresses. This instability appears to be qualitatively consistent with experimental observations of large depressions in the particle shape prior to splitting [6]. The existence of a splitting mechanism implies that there are conditions under which there is no single equilibrium shape for an isolated precipitate. This may prove useful in finding situations in which elasticity can favor an array of equally sized precipitates.

Splitting instabilities driven by applied fields have been observed previously in simulations of Lee [26] and Li and Chen [13]. Lee's simulations shows splitting that appears to proceed by a continuous instability of the particle shape, similar to the simulations presented here. In contrast, Li and Chen's simulations indicate that while morphological changes such as nonconvex particle shapes are observed during the splitting process, a major element of the splitting occurs by the particle hollowing out from the center

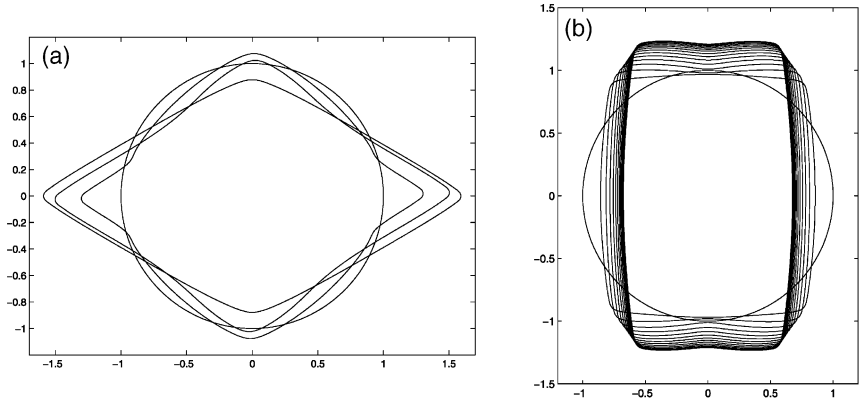

Fig. 13. The evolution of Ni_3Ga precipitates with tetragonal misfit, Z=5 and applied stress. The misfit is $\varepsilon_{11}^T = 1.3$, $\varepsilon_{22}^T = 1$ and $\varepsilon_{12}^T = 0$. In (a), the applied stress is $\sigma_{11}^0 = 1$, $\sigma_{22}^0 = -1$ and $\sigma_{12}^0 = 0$, while in (b), $\sigma_{11}^0 = -1$, $\sigma_{22}^0 = 1$ and $\sigma_{12}^0 = 0$.

prior to splitting. However, our results compare well to Li and Chen's results on the direction of the splitting.

The onset and direction of the instability depend on the magnitude of both the misfit strain and applied stress as well as the details of the applied stress, the elastic constants of both phases, and the initial shape of the particle. In principle, it should be possible to theoretically identify a set of elastic parameters that give rise to a morphological instability and hence predict the direction of the instability, see for example [38]. This has proven difficult in general, as the interactions among the many parameters are complicated. One alternative for elastically soft particles is to use the observation that the necking rate is a constant provides a simple means to predict the onset of instability when only one parameter is varied. That is, for a given precipitate-matrix system, one can fix Z and vary the magnitude of the applied stress to extrapolate the value at which the necking rate is zero; this gives an accurate estimate of the critical value of the applied stress for instability. Correspondingly, one could alter Z while holding the applied stress fixed to determine a critical value for Z. Estimates of the critical parameters using necking rates has proven to be fairly accurate for soft particle simulations. Because the necking rate is not constant for hard particles, this simple method of predicting critical parameters is not appropriate in that case.

In simulations in which splitting occurs because of non-dilatational applied stresses, it is clear that elastic inhomogeneity is also required. It is easily shown that if the system is elastically homogeneous, that part of G^{el} (in equation (14)) arising from the applied fields will be constant along the interface, and so will not affect the particle shape. We have found in the simulations that the strength of the elastic fields required for instability increases as the amount of inhomogeneity decreases. If we consider the evolution of a particle with the elastic constants of Ni_3Al, which are only slightly lower than those of Ni, we find (for otherwise identical parameters) instabilities that look similar to those seen in the NiGa system, but which require a value of Z roughly twice that for Ni_3Ga.

In real systems, applied stress could arise during processing. Elastic interactions among particles may play a similar role as applied stress in determining the evolution of a given particle. However, we have never seen evidence of splitting-type behavior in multi-particle simulations in the absence of applied stress. This suggests that high stresses may be needed to generate splitting. It is straightforward to use the simulation results to determine the magnitude of stress required to generate splitting in real alloys. For example, based on [39–42], reasonable estimates for system parameters in Nickel-based alloys are $C_{66}^M = 100$ GPa, $\varepsilon_{11}^T = \varepsilon_{22}^T = 0.005$, $\gamma = 0.025$ J/m^{2}and $R = 0.25\times10^{-6}$ m. This yields a value of $Z = 25$ and a stress scaling $C_{66}^M \epsilon_{22}^T = 500$ MPa. Recalling that a dimensionless applied shear of about 0.2 generated an instability for $Z = 25$, we estimate the critical stress to be on the order of 100 MPa, which may be near the limit of the elastic regime. While the exact value of the critical stress depends on Z, the elastic constants, the stress state and the initial shape, we note that our estimate is consistent with the 80 MPa stress used in Li and Chen's simulations to generate splitting of a single particle [13].

All of our observations of particle splitting involved one particle splitting into two (or in one case three) particles. While we have observed some non-convexity on all four sides of the particles, as in Fig. 1, we have never observed splitting into four particles. This is in contrast to the work of [13, 23, 26]. There is experimental evidence of eight-fold splitting, which seems to occur by instabilities arising on the three pairs of faces of a cuboidal precipitate [6]. It is possible that this is a three-dimensional phenomenon that cannot be captured by two-dimensional simulations. Energy calculations show that splitting of a cube into an octet of smaller cubes can reduce the elastic energy of the system more than splitting into

two plates [11, 43]. On the other hand, the higher surface energy associated with octets over plates would favor splitting into plates.

While we have a good picture of precipitate evolution in the presence of non-dilatation applied stress, the picture is less clear when we consider non-dilatational misfit strains. We expected, based on the linear analysis of [38] and the equivalent inhomogeneity concept of Eshelby [44], that non-dilatational misfit strains and applied stresses would give similar behavior, and in particular would both generate splitting. Instead, we have found that non-dilatational misfits generate non-convex shapes, as has been previously observed in equilibrium shape calculations [45, 16]. We cannot, however, conclusively argue that the non-convex precipitates will eventually split. The tetragonal misfit strain considered in Fig. 13 appears to have stabilized the shape, as the applied stress in that case would, by itself, lead to a splitting instability. Indeed, the combined presence of applied stress and tetragonal misfit appears to cause strong faceting, which may be a factor in the stabilization. This faceting, and especially the associated sharp corners, also makes it difficult to track the long-time evolution of the particle.

Acknowledgements—The authors thank J.K. Lee for many interesting and useful conversations. They also thank the Minnesota Supercomputer Institute for its support through a Supercomputer Resource Grant. JL thanks the Institute for Mathematics and its Applications for their hospitality while he avoids cleaning his office. QN acknowledges support from the NSF through grant DMS0074414. JL also acknowledges support from the NSF.

REFERENCES

1. Ardell, A. J. and Nicholson, R. B., *Acta metall.*, 1966, **14**, 1295.
2. Maheshwari, A. and Ardell, A. J., *Scripta metall.*, 1992, **26**, 34712.
3. Calderon, H. A., Kostorz, G., Qu, Y. Y., Dorantes, H. J., Cruz, J. J. and Cabanas-Moreno, J. G., *Mat. Sci. Eng. A*, 1997, **238**, 13.
4. Miyazaki, T., Hakamura, K. and Mori, H., *J. Mater. Sci.*, 1979, **14**, 1827.
5. Tien, J. K. and Copley, S. M., *Metall. Trans.*, 1971, **2**, 215.
6. Yoo, Y. S., Yoon, D. Y. and Henry, M. F., *Metals and Mat.*, 1995, **1**, 47.
7. Johnson, W. C., *Metall. Trans.*, 1987, **18A**, 233.
8. Johnson, W. C. and Cahn, J. W., *Acta metall.*, 1984, **32**, 1925.
9. Jou, H. -J., Leo, P. H. and Lowengrub, J. S., *J. Comp. Phys.*, 1997, **131**, 109.
10. Leo, P. H., Lowengrub, J. S. and Nie, Q., *J. Comp. Phys.*, 2000, **157**, 44.
11. Khachaturyan, A. G., Semenovskaya, S. V. and Morris, J. W. Jr, *Acta metall.*, 1988, **36**, 1563.
12. Lee, J. K., *Metal Trans.*, 1996, **27A**, 1449.
13. Li, D. Y. and Chen, L. Q., *Acta mater.*, 1999, **47**, 247.
14. McCormack, M., Khachaturyan, A. G. and Morris, J. W., *Acta metall.*, 1992, **40**, 325.
15. Orlikowski, D., Sagui, C., Somoza, A. and Roland, C., *Phys. Rev. B*, 1999, **59**, 8646.
16. Schmidt, I. and Gross, D., *J. Mech. Phys. Solids*, 1997, **45**, 1521.
17. Socrate, S. and Parks, D. M., *Acta metall.*, 1993, **41**, 2185.
18. Su, C. H. and Voorhees, P. W., *Acta mater.*, 1996, **44**, 1987.
19. Wang, Y., Chen, L. Q. and Khachaturyan, A. G., *Acta metall.*, 1993, **41**, 279.
20. Wang, Y. and Khachaturyan, A. G., *Acta metall.*, 1995, **43**, 1837.
21. Doi, M., Miyazaki, T. and Wakatsuki, T., *Mater. Sci. and Eng.*, 1985, **74**, 139.
22. Miyazaki, T., Imamura, H. and Kozakai, T., *Mater. Sci. and Eng.*, 1982, **54**, 9.
23. Zhang, J. D., Li, D. Y. and Chen, L. Q., in *Phase transformations and systems driven far from equilibrium*. MRS, 1998, **481**, 243.
24. Lee, J. K., *Metals and Materials*, 1996, **2**, 183.
25. Lee, J. K., *Int. Materials Rev.*, 1997, **42**, 221.
26. Lee, J. K., *Theoretical and applied fracture mechanics*, 2000, **33**, 207.
27. Leo, P. H. and Sekerka, R. F., *Acta metall.*, 1989, **37**, 3119.
28. Leo, P. H., Lowengrub, J. S. and Jou, H. -J., *Acta mater.*, 1998, **46**, 1213.
29. Greenbaum, A., Greengard, L. and McFadden, G. B., *J. Comp. Phys.*, 1993, **105**, 267.
30. Green, A. E., *Phil. Mag.*, 1943, **34**, 416.
31. Rizzo, F. J. and Shippy, D. J., *J. Composite Mater.*, 1970, **4**, 36.
32. Schmidt, I. and Gross, D., *Arch. Mech.*, 1995, **47**, 379.
33. Schmidt, I., Mueller, R. and Gross, D., *Mechanics of Materials*, 1998, **30**, 181.
34. Mikhlin, S. G., *Integral Equations and their Applications to Certain Problems in Mechanics, Mathematical Physics and Technology*. Pergamon, 1957.
35. Saad, Y. and Schultz, M. R., *SIAM J. Sci. Stat. Comput.*, 1986, **7**, 856.
36. Sidi, A. and Israeli, M., *J. Sci. Comp.*, 1988, **3**, 201.
37. Hou, T. Y., Lowengrub, J. S. and Shelley, M. J., *J. Comp. Phys.*, 1994, **114**, 312.
38. Leo, P. H. and Jou, H. -J., *Acta metall.*, 1993, **41**, 2271.
39. Ardell, A. J., *Interface Sci.*, 1995, **3**, 119.
40. Prikhodko, S. V., Carnes, J. D., Isaak, D. G. and Ardell, A. J., *Scripta mater.*, 1997, **38**, 67.
41. Kamara, A. B., Ardell, A. J. and Wagner, C. N. J., *Met. Trans.*, 1996, **27A**, 2888.
42. Hirata, T. and Kirkwood, D. H., *Acta metall.*, 1977, **25**, 1425.
43. Leo, P. H. and Muller, S., *Modelling Simul. Mater. Sci. Eng.*, 1999, **7**, 939.
44. Eshelby, J. D., in *Progress in Solid Mechanics 2*, ed. I. N. Sneddon and R. Hill. North-Holland, Amsterdam, 1961, p. 89.
45. Thompson, M. E., Su, C. S. and Voorhees, P. W., *Acta metall.*, 1994, **42**, 2107.

APPENDIX A

A.1. Normalized variables

We briefly present the relevant normalizations for the diffusion and elasticity problems. We use tildes to denote dimensional quantities and we drop the tildes for dimensionless quantities. For a more complete discussion, see Appendix 1 in reference [9].

The normalization of the diffusion problem is based on choosing an arbitrary length scale $\tilde{L}_0$. This length scale is in general chosen to be proportional to the square root of the precipitate area. We normalize the composition c in the matrix as

$$u = \frac{c - c_0}{\Lambda}$$

Here, c is the dimensionless mole fraction of diffusing species in the matrix, and $\tilde{c}^0$ is a reference composition in the matrix corresponding to a flat interface with no elasticity. Also,

$$\Lambda = \frac{c_0 \tilde{\zeta} \tilde{\tau}}{\tilde{L}_0}$$

is a dimensionless parameter that comes from the full derivation of the modified Gibbs-Thomson equation (2), where $\tilde{\zeta}$ is a constant that depends on the thermodynamics of the particular system (see [9]) and $\tilde{\tau}$ is the surface energy.

We also chose a time scale

$$\tilde{T} = \frac{\tilde{L}_0^2(\Gamma_P - \Gamma_I)}{\tilde{D}}$$

with $\Gamma_p = (c^P - c_0)/\Lambda$, $\Gamma_I = (c^{MI} - c_0)/\Lambda$, and where c^P is the (constant) mole fraction of diffusing species in the precipitate and c^{MI} is the mole fraction in the matrix at the precipitate-matrix interface. The length and time scales can be used to define a dimensionless normal velocity of the interface,

$$V = \frac{\tilde{V}\tilde{T}}{\tilde{L}_0}$$

The normalization of the elasticity problem is based on scaling all elastic constants by $\tilde{C}_{66}^M$ (using Voight notation), all strains by ε_{22}^T, and all stresses by $\tilde{C}_{66}^M \varepsilon_{22}^T$; i.e.,

$$C_{ij}^{\cdot} = \tilde{C}_{ij}^{\cdot}/\tilde{C}_{66}^M$$

$$\varepsilon_{ij}^{\cdot} = \varepsilon_{ij}^{\cdot}/\varepsilon_{22}^T$$

$$\sigma_{ij}^{\cdot} = \sigma_{ij}^{\cdot}/(\tilde{C}_{66}^M \varepsilon_{22}^T).$$

Finally, the parameter Z is given by

$$Z = \tilde{C}_{66}^M (\varepsilon_{22}^T)^2 \tilde{L}_0/\tilde{\tau} \tag{A1}$$

and so is simply the ratio of the elastic energy scaling $\tilde{C}_{66}^M(\varepsilon_{22}^T)^2$ to the surface energy scaling $\tilde{\tau}/\tilde{L}_0$.